NANO LETTERS

Letter

pubs.acs.org/NanoLett

Suppressing Nucleation in Metal–Organic Chemical Vapor Deposition of MoS_2 Monolayers by Alkali Metal Halides

HoKwon Kim,[†,‡] Dmitry Ovchinnikov,[†,‡] Davide Deiana,[§] Dmitrii Unuchek,[†,‡] and Andras Kis*[,†,‡]

[†]Electrical Engineering Institute, École Polytechnique Fédérale de Lausanne (EPFL), CH-1015 Lausanne, Switzerland

[‡]Institute of Materials Science and Engineering, École Polytechnique Fédérale de Lausanne (EPFL), CH-1015 Lausanne, Switzerland

[§]Interdisciplinary Center for Electron Microscopy (CIME), École Polytechnique Fédérale de Lausanne (EPFL), CH-1015 Lausanne, Switzerland

S *Supporting Information*

ABSTRACT: Toward the large-area deposition of MoS_2 layers, we employ metal–organic precursors of Mo and S for a facile and reproducible van der Waals epitaxy on c-plane sapphire. Exposing c-sapphire substrates to alkali metal halide salts such as KI or NaCl together with the Mo precursor prior to the start of the growth process results in increasing the lateral dimensions of single crystalline domains by more than 2 orders of magnitude. The MoS_2 grown this way exhibits high crystallinity and optoelectronic quality comparable to single-crystal MoS_2 produced by conventional chemical vapor deposition methods. The presence of alkali metal halides suppresses the nucleation and enhances enlargement of domains while resulting in chemically pure MoS_2 after transfer. Field-effect measurements in polymer electrolyte-gated devices result in promising electron mobility values close to 100 $cm^2\ V^{-1}\ s^{-1}$ at cryogenic temperatures.

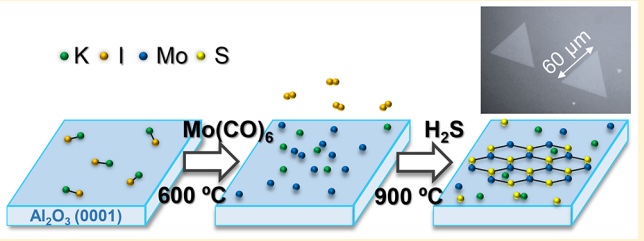

KEYWORDS: *Chemical vapor deposition, two-dimensional transition metal dichalcogenides, nucleation and growth, microstructure engineering, FET devices*

The chemical vapor deposition of two-dimensional materials is a highly promising method to produce atomically thin layers at a large scale for harnessing their attractive properties. Monolayer MoS_2 is a model 2D semiconductor that can be used to realize field-effect transistors with high current on/off ratios.[1] It is a naturally occurring material with a good chemical stability that exhibits a wide range of attractive properties such as a spin–orbit coupling-induced band splitting,[2,3] a mechanically tunable bandgap,[4−8] and a low temperature superconductivity.[9−13]

Toward the large-scale synthesis of MoS_2 thin films, a conventional chemical vapor deposition method of producing MoS_2 monolayers typically involves low vapor pressure solid powder precursors such as MoO_3 and sulfur. It has been investigated for centimeter-scale deposition of polycrystalline monolayer MoS_2 with grain sizes of nanometer to micrometer and with controllable coverage.[14,15] However, low vapor pressures of the solid precursors require them to be loaded inside a heated zone of the reactor chamber leading to a limited control over the vapor phase composition and deposition rate. Thus, this synthesis approach heavily undermines the ability to control the nucleation density, thickness, and coverage.

Here, we aim to address this issue by employing well-known metal–organic precursors of molybdenum, $Mo(CO)_6$, which is a high vapor pressure solid, and of sulfur, H_2S in gas phase.[16−19] This metal-organic chemical vapor deposition (MOCVD) approach allows reliably setting the concentration of precursor gases within the gaseous mixture that is transported to the substrate by controlling the evaporation rates of the solid precursor and mass flow rates. An extensive vapor phase thermodynamics study performed by Kumar et al.[19] has shown that growth temperatures above 850 °C at atmospheric pressure lead to layer-by-layer growth of MoS_2 without extraneous deposition of carbon contaminants resulting from the organic ligands of the precursor.

Although previous studies have paved the way to growing atomically thin films of MoS_2 by MOCVD, the underlying MOCVD growth mechanism and ways to control the critical parameters that determine the quality of the deposited film such as coverage and domain sizes are still lacking. In this work, we show that pre-exposing the substrate before the growth stage to nucleation suppressors such as alkali metal halides, together with the Mo precursor, is an important factor in decreasing the nucleation density and enabling large-area growth of MoS_2 domains on the order of 10 μm within a short growth time of 30 min. This is a significant improvement over the growth morphology obtained without the use of the alkali metal halides and offers a reproducible and cost-effective

Received: June 1, 2017
Revised: July 7, 2017
Published: July 12, 2017

DOI: 10.1021/acs.nanolett.7b02311
Nano Lett. XXXX, XXX, XXX−XXX

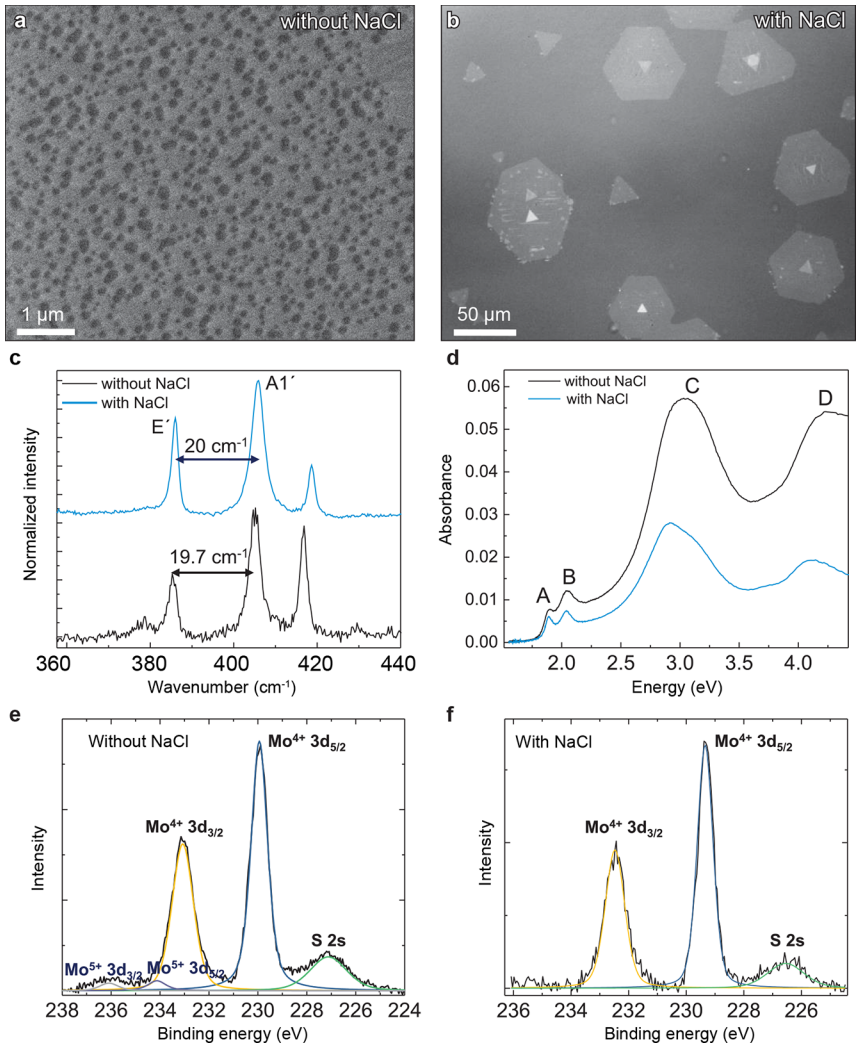

Figure 1. (a) SEM image of MoS_2 nuclei on c-sapphire obtained from an alkali metal halide-free growth. The dark, round-shaped domains are MoS_2 islands that randomly nucleated on the surface of sapphire, which appears as a bright background in the image. (b) Optical microscope image of MoS_2 grown on sapphire during NaCl-assisted growth. Note that optical microscopy was used in panel b instead of SEM to give a larger view of the sample and that MoS_2 layers appear to be brighter than the substrate. (c) Raman spectra of MoS_2 samples produced in the alkali−metal halide free process (bottom) and NaCl-assisted growth (top). (d) Absorbance spectra of the samples produced from the alkali−metal halide free process (black) and NaCl-assisted growth (blue). (e, f) Background-subtracted XPS core-level Mo 3d and S 2s spectra of the samples produced from the alkali-metal halide free process (e) and NaCl-assisted growth (f). Gauss-Lorenztian mixed peak fitting analysis was performed on the spectra to determine the chemical states of the deposited film.

way for mass-scale production of microstructure-engineered two-dimensional transition metal dichalcogenides (TMDCs).

Results and Discussion. We first employed a single-growth-step procedure similar to Kumar et al.[19] in a quartz tube, with a hot-wall furnace setup (Figure S1), releasing both precursors at the same growth stage at a fixed growth temperature and without using any alkali metal halides. This growth procedure leads to a deposition of finely grained, circularly shaped MoS_2 nuclei on sapphire with a high nucleation density and an average grain-to-grain distance of less than 100 nm for a wide range of growth temperatures (Figure 1a and Supporting Information, SI, Figure S2). Figure S2 shows the evolution of growth morphology of MOCVD MoS_2 on sapphire as a function of the growth temperature. The higher growth temperature leads to reduced nucleation density and thus larger grain sizes. This nucleation density *versus* T_{growth} behavior (Figure S2b) is exponential in nature due to thermally activated processes that lead to random nucleation of MoS_2 arising from the collective crystallization of surface adatoms.[20]

Raman and UV−vis absorbance spectra (Figure 1c,d) measured over multiple grains on sapphire indicate that MoS_2 is largely of monolayer nature and has good optical quality. The peak parameters and relative distances of E′ and A_1' peaks of Raman spectra correspond to those of monolayer MoS_2.[21] A representative absorbance spectra for the growth temperature of 950 °C is shown in Figure 2d where clear features of A, B, C, and D excitons can been seen.[22−25,15] Furthermore, the core-level XPS spectra of Mo 3d (Figure 1e) indicate that the MOCVD growth results in MoS_2 with a small amount of peaks arising from Mo^{6+} oxidation state akin to that of MoO_3, which could be originating from a slight oxidation of the sample around the grain boundaries or other defects.[26]

To reduce the density of nuclei and improve their lateral size, we placed alkali metal halides (mainly KI or NaCl) upstream as first employed by Kang et al.[18] It has been suggested that the

DOI: 10.1021/acs.nanolett.7b02311
Nano Lett. XXXX, XXX, XXX−XXX

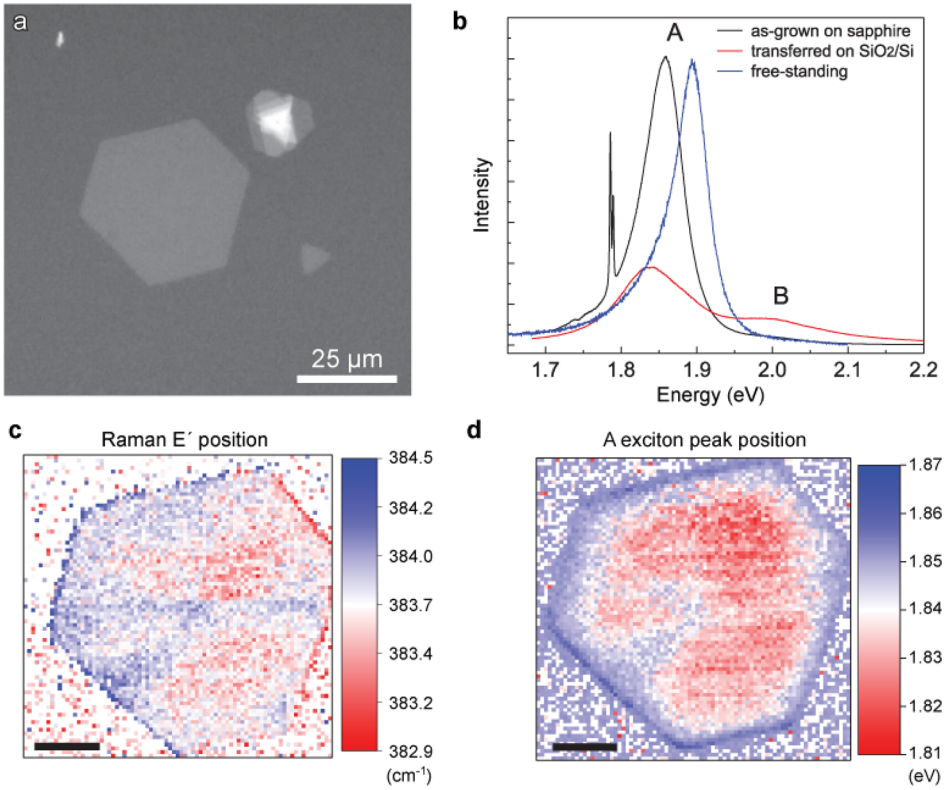

Figure 2. (a) Optical microscope image of an MoS_2 island grown on sapphire after KI-assisted MOCVD. (b) Room-temperature PL spectra of as-grown MoS_2 on sapphire, transferred onto SiO_2/Si, and free-standing MoS_2 transferred onto a TEM grid (normalized to as-grown on sapphire spectra). (c) E′ Raman peak position map of the island constructed after multipeak fitting of the MoS_2 Raman spectral region for each pixel. (d) PL maximum peak position map of the MoS_2 island. Scale bars, 5 μm (c and d).

presence of the alkali halides would reduce the concentration of water in the vapor phase environment of the MOCVD system encouraging the two-dimensional growth of nuclei while suppressing nucleation. We found that a pre-exposure of the sapphire substrate to $Mo(CO)_6$ together with a very small amount of KI (<1 mg) placed in front of the substrate prior to the growth stage is enough to significantly boost the domain sizes of MoS_2 beyond 10 μm (Figure 1b and Figure S3), which is more than a 2 orders of magnitude improvement over the one-growth-step approach on the nuclei size (~100 nm vs ~50 μm at T_{growth} = 950 °C) and similar to that of conventional CVD involving $MoO_{3(s)}$ and $S_{(s)}$ precursors. Large-area Raman (Figure 1c) and absorbance (Figure 1d) measurements demonstrate that the resulting film also exhibits good crystalline characteristics.[15]

The nucleation density and coverage appear to be limited by the amount of Mo as shown in Figure S3. The growth time beyond 30 min (Figure S3g,h) did not significantly influence the nucleation density and coverage, suggesting a quick growth rate and Mo-limited growth. Further increasing further the exposure to Mo increased the nucleation density and coverage, however, it led to the decrease in the domain size (Figure S3f). This significantly improved grain size allows us to carefully investigate a single, individual island of MoS_2 at a larger spatial scale. For instance, room temperature PL spectra (Figure 2b) of the as-grown island on sapphire exhibit a strong emission coming from the A exciton, characteristic of the direct band gap of monolayer MoS_2.[22,25] The fwhm of ~64 meV is comparable to as-grown monolayer MoS_2 samples on sapphire produced by conventional CVD method and suggests a high quality with a relatively small defect concentration. To probe the spatial inhomogeneity of the island, Raman and PL mapping was performed on the same area. Especially, the positions of the E′ Raman peaks and excitonic PL peak maxima appear to shift most prominently as illustrated in Figure 2c and d. Both of the maps follow a similar pattern with band-like regions of red-shifted peaks appearing to be radiating outward from the center of the island. This variation in peak positions can be attributed to a nonuniform strain field within the island where parts of the island pinned to the substrate are in tensile strain due to the difference in the thermal expansion coefficient while some parts are relaxed during the sample cooling.[8,15] On the basis of the distributions of the E′ peak position and PL max. position values, a tensile strain difference of ~0.3% was estimated, which is consistent with the E′ position shift of a sample after a transfer onto a c-sapphire substrate (Figure S4a), and what is expected from the thermal expansion coefficient mismatch between bulk MoS_2 and sapphire.[8,15]

For chemical state analysis, micro-XPS was performed on the islands before and after transferring the entire film onto the SiO_2/Si substrate. From the survey spectra (Figure 3a), the main contaminant on the as-grown MoS_2 appears to be alkali metals originating from the alkali metal halides used for the growth. The core-level spectra indicate that, while there are alkali metals on top of the island or at the interface between the island and substrate, the oxidation states of Mo appear to correspond to those of MoS_2 islands (Mo^{4+}) where the small deviation is likely to be related to oxidized Mo states at the interface.

After transfer, the MoS_2 film no longer contains a significant amount of alkali metals (Figure 3b,c). It is apparent that the alkali metals were washed away in the solvents used during the

DOI: 10.1021/acs.nanolett.7b02311
Nano Lett. XXXX, XXX, XXX−XXX

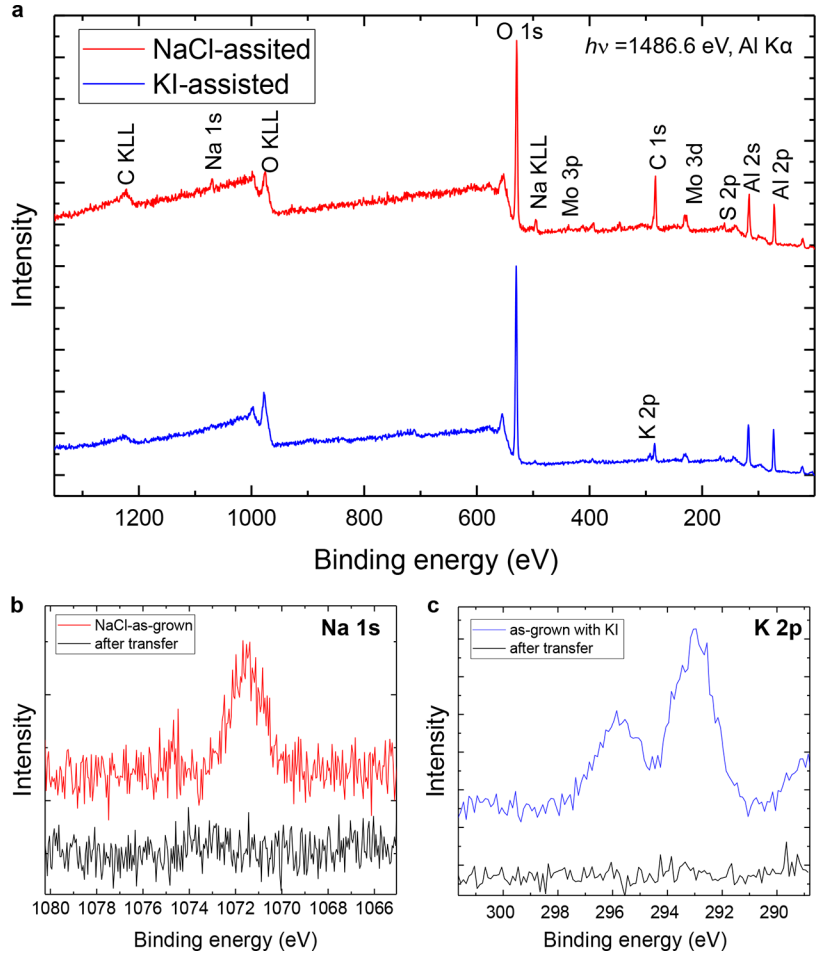

Figure 3. (a) XPS survey spectra of MoS_2 samples that were grown in the presence of NaCl and KI. (b) XPS core-level spectra of the Na 1s region for as-grown MoS_2 sapphire (top) obtained by NaCl-assisted growth and the transferred sample on SiO_2/Si substrate (bottom). (c) XPS core-level spectra of K 2p region containing K 2p3/2 and K 2p1/2 peaks for as-grown MoS_2 on sapphire (top) obtained by KI-assisted growth and sample transferred sample onto SiO_2/Si substrate (bottom).

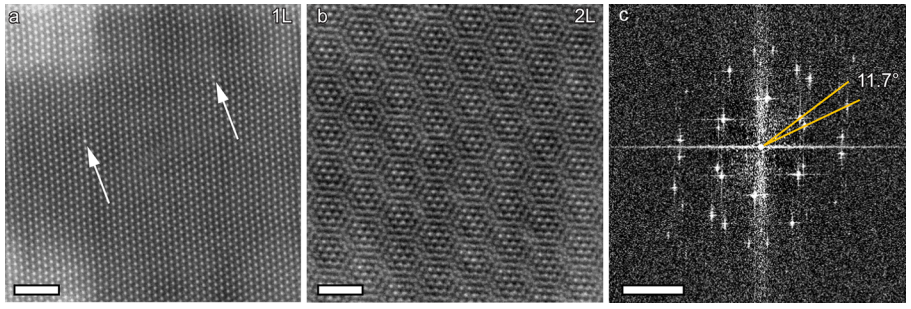

Figure 4. (a) High-resolution HAADF-STEM image of a monolayer MoS_2 imaged at 80 kV. The array of Mo atoms appears to be much brighter than sulfur atoms due to the Z contrast in HAADF-STEM mode. The white arrows indicate substitutional unintentional dopant atoms heavier than Mo. (b) High-resolution HAADF-STEM image of 2L MoS_2 area grown near the center of the island and (c) corresponding FFT image of the 2L superstructure of b. Scale bars, 2 nm (a, b); 4 nm^{-1} (c).

transfer process. Indeed, the examination of the sapphire substrate after the complete delamination shows no presence of potassium (Figure S5a–d). Additionally, in a separate experiment, we observe the removal of alkali metal after DI water washing of sapphire substrates that had been annealed in the atmosphere rich of alkali metal halides suggesting that the alkali metals interact only weakly with the substrate (Figure S5e–g).

Furthermore, the XPS core-level measurements (Figure S5b) show that residual Mo are bound more strongly to the sapphire as they still show a significant contribution from Mo^{5+} oxidation states which can be linked to a oxidized form of Mo at the interface between MoS_2 and sapphire that possibly participated in the growth process of MoS_2.

To take a closer look at the atomic structure, high-resolution HAADF-STEM imaging was carried out on freestanding MoS_2 layers transferred onto a TEM grid. Figure 4 illustrates a well-ordered MoS_2 atomic lattice apparently exhibiting an ideal 2H-phase lattice structure with a low defect and impurity

DOI: 10.1021/acs.nanolett.7b02311
Nano Lett. XXXX, XXX, XXX−XXX

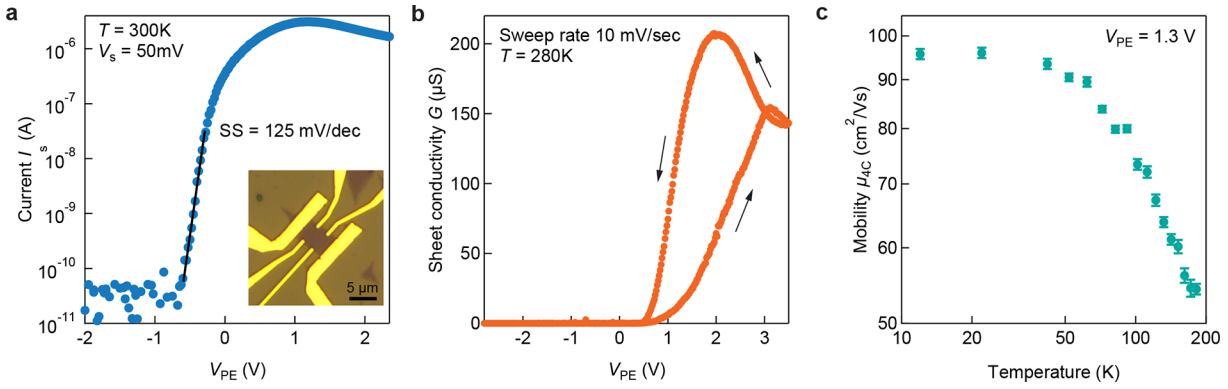

Figure 5. EDLT based on monolayer MOCVD MoS_2. (a) Transfer characteristics of a 4-probe electric double-layer transistor, recorded with a sweep rate of 5 mV/s. (Inset) Optical microscope image of a four-probe transistor device before electrolyte deposition. (b) Sheet conductivity at 280 K as a function of V_{PE}. The black arrows show the direction of gate voltage sweep with a 10 mV/s rate. (c) Temperature dependence of the four-probe field effect electron mobility values for V_{PE} = 1.3 V.

concentration. On the basis of the FFT analysis, the lattice spacing between the Mo atoms, which appear much brighter than sulfur atoms due to the Z contrast,[27] was calculated to be 3.2 Å, matching closely with the known values of the MoS_2 lattice parameter.[25,28] Occasionally, bright substitutional dopants could be observed in place of Mo atoms in the atomic scale images. This heavier element is likely tungsten, which was the most significant impurity in the Mo precursor used according to the impurity analysis provided by the supplier (lot no. MKBX7702 V, Sigma-Aldrich) as also detected by the large-area STEM-EDS measurements (Figure S6). Again, no significant alkali metals (Na or K) and halides (Cl or I) were observed in the MoS_2 area, consistent with the XPS observation. Indeed, the PL measurements on the free-standing monolayer MoS_2 (Figure 3b) show a strong exciton A peak with a minimum trion peak contribution with the fwhm of ∼45 meV, similar to the best values of A exciton fwhm (∼47−50 meV[22,25,29−31]) for room-temperature PL of free-standing monolayer MoS_2 found in the literature. Moreover, low-temperature photoluminescence spectra of a transferred sample taken at 4 K (as shown in Figure S4b) exhibit no significant bound exciton peak at lower energies, which are normally found for CVD-grown MoS_2 monolayers and likely arises from trapped charges or defects.[32,33]

Sometimes, stacks of bi- to few-layer MoS_2 could be observed at the centers of individual islands. This is a common feature for significantly lowered nucleation density resulting in well-isolated domains (internucleus distance ≫ surface diffusion length of the active species)[34] at a high growth temperature and large amount of salts. The high-resolution STEM image indeed shows that a bilayer found near the center of an island can have a random twisting angle as evident from a FFT analysis (e.g., Figure 4c). This unusual stacking and weak interaction between the layers were also evidenced by Raman and photoluminescence spectra in Figures S4c and d.

For the electrical characterization of our material, MOCVD MoS_2 was transferred onto degenerately doped Si substrates with a 270 nm thick, thermally grown SiO_2 layer. First, we performed characterization of our samples using the solid back-gate in vacuum after *in situ* annealing, which established the n-type charge conduction. The sheet resistivity and contact resistance were not low enough to observe band-like transport (Figure S7a,b) possibly due to the intrinsically low doping level of our sample. To this end, we used polymer electrolyte (PE) gating to build electric double-layer transistors (EDLTs) based on monolayer MoS_2 and explore a wide range of carrier densities. [EMIM][TFSI] in PS−PMMA−PS polymer matrix[35−37] was spin-coated onto our samples followed by baking of the samples in high vacuum for 2 h at 70 °C. Current I_s as a function of polymer electrolyte voltage V_{PE} is shown in Figure 5a for one sweep. We observe a sharp turn on with a subthreshold slope (SS) value of 125 mV/dec at room temperature, in line with measurements performed at 240 K in monolayer CVD MoS_2 grown from MoO_3 and solid sulfur precursors.[32] The dome-like shape at high V_{PE} values is related to electrolyte-induced disorder.[37−39] Hysteresis is present in our measurements, but overall we found good reproducibility in three devices that were measured. In Figure 5b we show sheet resistance extracted at a lower temperature (T = 280 K). For further insights into transport properties, we performed temperature-dependent measurements (Figure 5c) applying fixed V_{PE} at 280 K, lowering temperature below freezing point of PE (220−240 K) and turning on the back gate. We found low contact resistances with PE gating down to low temperatures (Figure S7b). Band-like transport could be achieved in contrast to solid-gated samples (e.g., Figure S7c), after a metal−insulator-transition above the critical conductivity of e^2/h, to yield a four-probe electron mobility, $\mu_{4C} \sim 95$ cm^2/(V s) at T = 12 K. This behavior is in agreement with early reports of band-like transport in exfoliated[40] and CVD-grown monolayer MoS_2.[41] We noticed that the low temperature mobility is limited by electrolyte-induced disorder.[39] A similar trend could be observed for example comparing PE-gated[38] and h-BN encapsulated[42] monolayer WSe_2 devices. Overall, we have demonstrated good electrical performance of our devices.

We now turn our attention to the growth mechanism and the effect of the alkali metal halides on domain size enlargement. It is not likely that the alkali metal halides actually lower the amount of residual water vapor, which could affect the two-dimensional growth,[43] as originally suggested by Kang et al. for a low-temperature, low-pressure MOCVD process,[18] since very small amounts (0.1−1 mg) were used so that most of the salt evaporated or decomposed before the actual growth stage. Furthermore, when a large quantity of salt was placed upstream, away from the heating zone of the furnace preventing the evaporation (Figure S8a), nucleation was not significantly suppressed. We have also investigated the effects of other ionic salts such as $CaCl_2$ and CaO which are known to be more

DOI: 10.1021/acs.nanolett.7b02311
Nano Lett. XXXX, XXX, XXX−XXX

effective desiccating agents than the alkali metal halides.[44,45] However, we did not observe significant suppression of the nucleation density (Figure S8b,c).

Instead of acting as desiccants, the alkali metal halides are more likely to act in a similar way as planar, cyclic seeding promoters such as perylene-3,4,9,10-tetracarboxylic acid tetrapotassium salt (PTAS), 3,4,9,10-perylene tetracarboxylic acid dianhydride (PTCDA), and copper hexadecafluoro-phthalocyanine ($F_{16}CuPc$) that are known to suppress nucleation and enhance two-dimensional growth in the conventional chemical vapor deposition of TMDCs.[14,46−50] However, the underlying mechanism is not well-understood partly due to the complexity of the chemical vapor deposition process. Many factors such as nuclei surface/interfacial/edge energy, surface diffusion rate, active species attachment rate, and density of preferential nucleation sites are expected to greatly influence the nucleation density on a substrate. One possible explanation is that a planar molecule can act as a seeding promoter because it can stabilize the two-dimensional nuclei due to its geometry.[48] Recently, an atomic additive such as Cu was also shown to promote the two-dimensional growth by attaching itself preferentially on top of the hexagonal lattice, rather than at edge sites, blocking the three-dimensional growth during CVD of TMDCs.[51] We believe that alkali metal halides can also act in a similar way to enhance two-dimensional growth versus nucleation.

Additionally, a small intentional amount of oxygen has been shown to suppress nucleation of graphene[52,53] and TMDCs in CVD by rendering potential nucleation sites less active or by increasing the size of the critical nucleus. In the case of alkali metal halides, the excessive amount of alkali metal (≫10 mg) indeed appears to decrease the coverage as well as nucleation of MoS_2 layers (e.g., Figure S8a). The shapes of nuclei changed from circular to more faceted (Figure 1a, b), assuming a triangular or hexagonal shape with straight edges. In such case, the nucleation rate must have sufficiently slowed down so that the density of nucleation would not reach the point of saturation even toward the end of the growth stage.[20,54] This suggests that the alkali metal salts have likely induced a surface poisoning effect that would limit the nucleation and coverage.[34]

To further elucidate the effect of alkali metal halides, we interrupted the MOCVD process during a KI-assisted growth at the end of the $Mo(CO)_6$ exposure stage without introducing H_2S. XPS analysis shows that Mo and K were adsorbed on the surface after the exposure step while iodine is no longer present (Figure S5b). This adsorption of Mo could not be achieved under the same amount of $Mo(CO)_6$ exposure without the use of the alkali metal halide. Furthermore, in a separate experiment, $Mo(CO)_6$ was introduced at a temperature above 900 °C after evaporating away KI from the substrates where only K remains absorbed on the substrate. This did not lead to a significant deposition of Mo hinting us that both the alkali metal and halide have to be present. This is consistent with our observation that directly attempting a single-step approach with alkali metal salts did not lead to the enhancement of two-dimensional growth (Figure S9) likely due to the evaporation of salts at typical growth temperature ranges (850−1000 °C). In addition, we also tried the two-step approaches without any alkali metal halides or with a halogen-only environment by placing a boat or ampule of solid iodine upstream and repeated the growth experiment, but this lead to poor morphologies (e.g., Figure S8d). Therefore, these results show that the alkali metal halides play a dual role in facilitating adsorption of Mo in the pre-exposure stage and suppressing nucleation in the growth stage. Further work is underway to expand the parameter space and optimize the coverage and thickness uniformity.

Conclusion. We have developed a facile and reproducible method toward large-area growth of mono- to few-layer MoS_2 on c-sapphire using metal−organic precursors of Mo and S. The pre-exposure of growth substrates to alkali metal halides and the Mo precursor before the growth stage appears to play a crucial role in suppressing nucleation and increasing the lateral size of single-crystal domains from a few hundred nanometers to tens of microns. The MoS_2 film grown this way exhibits high crystallinity and good optoelectronic properties with a narrow A exciton and an electron mobility near 100 $cm^2V^{-1}s^{-1}$ at cryogenic temperatures in an electric double-layer transistor configuration. The XPS and STEM analysis has shown that the alkali metal halides do not bind strongly to the MoS_2 resulting in chemically pure MoS_2 after transfer. Our work is a major step toward advancing the microstructure engineering and large-area production of layered transition metal dichalcogenides.

Materials and Methods. *Metal−Organic Chemical Vapor Deposition System.* The metal−organic chemical vapor deposition system consists of a typical quartz tube three-zone hot wall furnace (Carbolite HZS 12/600) with gas flow rates controlled by mass flow controllers. High-purity H_2S and Ar gases were provided by compressed gas cylinders (Carbagaz). $Mo(CO)_6$ solid precursor (Sigma-Aldrich 577766, >99.9% purity) was loaded inside a stainless steel cylindrical bubbler (Strem Chemicals, Inc.) in a temperature controlled thermostat (Lauda Eco Silver) with a reverse bubbler configuration packed within silica beads 2 mm in diameter to facilitate the evaporation of $Mo(CO)_6$ by increased surface area.[55]

Before a typical growth step, the c-sapphire substrates ($Al_2O_3(0001)$) purchased from MTI Corp. were preannealed in air at 1000 °C for 1 h to induce clean, atomically smooth steps.[56] The MOCVD process was performed in several stages. For an alkali-metal salt-free, single-growth-step MOCVD process, the substrates placed in the central zone of the furnace were first heated to the growth temperature of 700−1020 °C under Ar atmosphere. We then introduced 1−3 sccm of H_2S into the quartz tube to create a sulfur-rich atmosphere in which the substrates were annealed for 15 min. After this, $Mo(CO)_6$ was introduced into the quartz tube using Ar carrier gas with an Ar flow rate of 1.5 sccm and a bubbler temperature of 5−20 °C which lead to the volumetric flow of 3.35×10^{-5} to 1.84×10^{-4} sccm of $Mo(CO)_6$ estimated using the reference values of temperature-dependent vapor pressure values and ideal gas law.[57] After 30−600 min of growth time (total $Mo(CO)_6$ exposure of 3.9−7.48 μg leading to the overall $Mo(CO)_6$ to H_2S molar ratio of ∼1:10 000 for the growth stage which ensures S-rich environment), $Mo(CO)_6$ flow was shut-off abruptly and the furnace allowed to cool to ambient temperature under the constant flow of H_2S and Ar in order to grow MoS_2 in a sulfur-rich environment.

For the alkali metal halide-assisted growth, 10 to 0.5 mg of KI or NaCl was placed upstream of the sapphire substrate support and loaded together with c-sapphire substrates (Figure S1a). The $Mo(CO)_6$ precursor was first introduced into the chamber when the temperature reached 600 °C, and the substrate was exposed to the precursor for 30 min (Figure S1b) for optimal adsorption of Mo. The substrate was heated to the growth temperature of 800−1050 °C for large-domain size

DOI: 10.1021/acs.nanolett.7b02311
Nano Lett. XXXX, XXX, XXX−XXX

growth in Ar wherein H_2S was introduced to initiate the sulfurization of the adsorbed Mo species. All other experimental configurations were kept the same as for the alkali metal halide-free growth.

Raman, Photoluminescence (PL), and Absorbance Measurements. Raman and PL measurements were performed using a Renishaw inVia confocal Raman microscope with an objective lens of ×100 and laser wavelength of 532 nm with a laser power (<0.3 mW) carefully adjusted for a minimal damage by checking to ensure that there are no peak shifts in the sample over repeated number of measurements. Diffraction gratings of 1200 g/mm and 600 g/mm were used for Raman and PL measurements, respectively, for suitable spectral ranges and resolution. Absorbance measurements were performed on an area approximately 1 cm in diameter using a Varian Cary UV/vis spectrophotometer.

X-ray Photoelectron Spectroscopy (XPS). For survey and core-level XPS analysis, ULVC-PHI Versa Probe II equipped with laboratory Al K-alpha X-ray source ($h\nu$ = 1486.6 eV) was used with a typical beam size of 200 μm for a survey and average-area analysis while a beam size of 20 μm was used for single-island analysis. A dual-beam charge neutralizer (low energy electron and He ion) was used on the insulating samples. The adventitious C 1s peak at the binding energy of 284.8 eV was taken as a reference for offsetting the raw spectra.

Atomic Force Microscopy (AFM) and Scanning Electron Microscopy (SEM) Imaging Techniques. AFM topographical imaging was performed with the Cypher Asylum Research atomic force microscope in amplitude modulation mode. SEM images were obtained by a field emission SEM Zeiss Merlin microscope with a charge neutralizer to image the as-grown sample on sapphire directly.

Scanning Transmission Electron Microscopy (STEM). High-resolution high-angle annular dark field (HAADF) scanning transmission electron microscopy (STEM) was performed in a double C_s-corrected FEI Titan Themis microscope equipped with a high brightness Schottky X-FEG electron source, a monochromator, and a SuperX energy-dispersive X-ray spectrometer (EDS), operated at 80 kV accelerating voltage and low electron beam current values (below 50 pA). The specimen for the STEM investigation was transferred on Si_3N_4 TEM windows (Norcada, Canada) with arrays of 2 μm diameter holes. Images were processed by Wiener filtering in Gatan Digital Micrograph software.

Transfer Method and Device Characterization. For transferring as-grown MoS_2 on sapphire, the sample was spin-coated with a polymer support of poly(methyl methacrylate) (PMMA) A2 1500 rpm for 1 min and was baked at 75 °C for 30 min. The edges of the sample were scratched by a diamond scriber for an efficient delamination of MoS_2/PMMA before it was immersed in the solution of KOH (30 wt %) at 70 °C for about 30 min. It was then taken out and gently placed onto DI water allowing the MoS_2/PMMA film to delaminate from the substrate and float on the DI water. The floating piece of the MoS_2/PMMA was transferred to three beakers of DI water to be fished out onto a target substrate [typically SiO_2 (270 nm)/Si for back-gated field effect measurements] which had been treated by a KOH solution (30 wt %) to render the surface hydrophilic to improve the adhesion. The transferred sample was left in acetone overnight and then annealed in a gaseous mixture of H_2 (10 v.%)/Ar at 380 °C for 4 h to remove PMMA.

The single crystalline area was chosen and etched in a rectangular Hall bar geometry for four contact measurements via e-beam lithography. Au was deposited using an e-beam evaporator with a thickness of 100 nm. [EMIM][TFSI] in the PS−PMMA−PS matrix was chosen as polymer electrolyte (PE) for gating. The solution was spin-coated on top of our devices, and a large area gate electrode was used to apply PE voltage, V_{PE}. Prior to measurements, the sample was baked in high vacuum for 2 h at 70 °C. For DC electrical measurements, we used Keithley 2400 SMU and Keithley 2000 DMM. Cryogenic measurements were performed in a Janis closed-cycle cryogen-free cryostat. Mobility measurements were performed in four-contact geometry, and a geometric back gate capacitance of 270 nm SiO_2 substrate 12.7 nF/cm^2 was used for mobility extraction below the freezing point of electrolyte (220−240 K). Interplay with the electrolyte gate could be excluded since the geometric capacitance was confirmed by Hall effect measurements in similar devices based on ReS_2.[37]

■ ASSOCIATED CONTENT

Supporting Information

The Supporting Information is available free of charge on the ACS Publications website at DOI: 10.1021/acs.nanolett.7b02311.

Supporting figures and electrical properties of monolayer MOCVD MoS_2 (PDF)

■ AUTHOR INFORMATION

Corresponding Author

*E-mail: andras.kis@epfl.ch.

ORCID

Andras Kis: 0000-0002-3426-7702

Notes

The authors declare no competing financial interest.

■ ACKNOWLEDGMENTS

We thank P. Mettraux (CIME, EPFL), A. Margez (MCP, EPFL), Z. Benes (CMI, EPFL), and F. Bobard (CIME, EPFL) for their training and technical support on XPS, Raman, e-beam lithography, and SEM systems, respectively. We thank D. Dumcenco for insightful discussion on the CVD processes. This project has received funding from the European Union's Horizon 2020 research and innovation programme under grant agreement no. 696656 (Graphene Flagship), European Union's Seventh Framework Programme FP7/2007-2013 under grant agreement no. 318804 (SNM), and Swiss SNF grant no. 153298 and was performed in the frames of the Marie Curie ITN network "MoWSeS" (grant no. 317451).

■ REFERENCES

(1) Radisavljevic, B.; Radenovic, A.; Brivio, J.; Giacometti, V.; Kis, A. *Nat. Nanotechnol.* **2011**, *6* (3), 147−150.
(2) Zhu, Z. Y.; Cheng, Y. C.; Schwingenschlögl, U. *Phys. Rev. B: Condens. Matter Mater. Phys.* **2011**, *84* (15), 153402.
(3) Liu, G.-B.; Shan, W.-Y.; Yao, Y.; Yao, W.; Xiao, D. *Phys. Rev. B: Condens. Matter Mater. Phys.* **2013**, *88* (8), 085433.
(4) *J. Chem. Phys.* **2014**, *140* (17), 174707.
(5) Yue, Q.; Chang, S.; Kang, J.; Zhang, X.; Shao, Z.; Qin, S.; Li, J. *J. Phys.: Condens. Matter* **2012**, *24* (33), 335501.
(6) Manzeli, S.; Allain, A.; Ghadimi, A.; Kis, A. *Nano Lett.* **2015**, *15* (8), 5330−5335.
(7) Pan, H.; Zhang, Y.-W. *J. Phys. Chem. C* **2012**, *116* (21), 11752−11757.

DOI: 10.1021/acs.nanolett.7b02311
Nano Lett. XXXX, XXX, XXX−XXX

(8) Lloyd, D.; Liu, X.; Christopher, J. W.; Cantley, L.; Wadehra, A.; Kim, B. L.; Goldberg, B. B.; Swan, A. K.; Bunch, J. S. *Nano Lett.* **2016**, *16* (9), 5836−5841.
(9) Costanzo, D.; Jo, S.; Berger, H.; Morpurgo, A. F. *Nat. Nanotechnol.* **2016**, *11* (4), 339−344.
(10) Saito, Y.; Nakamura, Y.; Bahramy, M. S.; Kohama, Y.; Ye, J.; Kasahara, Y.; Nakagawa, Y.; Onga, M.; Tokunaga, M.; Nojima, T.; Yanase, Y.; Iwasa, Y. *Nat. Phys.* **2015**, *12* (2), 144−149.
(11) Lu, J. M.; Zheliuk, O.; Leermakers, I.; Yuan, N. F. Q.; Zeitler, U.; Law, K. T.; Ye, J. T. *Science* **2015**, *350* (6266), 1353−1357.
(12) Roldán, R.; Cappelluti, E.; Guinea, F. *Phys. Rev. B: Condens. Matter Mater. Phys.* **2013**, *88* (5), 054515.
(13) Ge, Y.; Liu, A. Y. *Phys. Rev. B: Condens. Matter Mater. Phys.* **2013**, *87* (24), 241408.
(14) Lee, Y.-H.; Zhang, X.-Q.; Zhang, W.; Chang, M.-T.; Lin, C.-T.; Chang, K.-D.; Yu, Y.-C.; Wang, J. T.-W.; Chang, C.-S.; Li, L.-J.; Lin, T.-W. *Adv. Mater.* **2012**, *24* (17), 2320−2325.
(15) Dumcenco, D.; Ovchinnikov, D.; Marinov, K.; Lazić, P.; Gibertini, M.; Marzari, N.; Sanchez, O. L.; Kung, Y.-C.; Krasnozhon, D.; Chen, M.-W.; Bertolazzi, S.; Gillet, P.; Fontcuberta i Morral, A.; Radenovic, A.; Kis, A. *ACS Nano* **2015**, *9* (4), 4611−4620.
(16) Dhar, S.; Kumar, V. K.; Choudhury, T. H.; Shivashankar, S. A.; Raghavan, S. *Phys. Chem. Chem. Phys.* **2016**, *18* (22), 14918−14926.
(17) Dumcenco, D.; Ovchinnikov, D.; Sanchez, O. L.; Gillet, P.; Alexander, D. T. L.; Lazar, S.; Radenovic, A.; Kis, A. *2D Mater.* **2015**, *2* (4), 044005.
(18) Kang, K.; Xie, S.; Huang, L.; Han, Y.; Huang, P. Y.; Mak, K. F.; Kim, C.-J.; Muller, D.; Park, J. *Nature* **2015**, *520* (7549), 656−660.
(19) Kumar, V. K.; Dhar, S.; Choudhury, T. H.; Shivashankar, S. A.; Raghavan, S. *Nanoscale* **2015**, *7* (17), 7802−7810.
(20) Robinson, V. N. E.; Robins, J. L. *Thin Solid Films* **1974**, *20* (1), 155−175.
(21) Lee, C.; Yan, H.; Brus, L. E.; Heinz, T. F.; Hone, J.; Ryu, S. *ACS Nano* **2010**, *4* (5), 2695−2700.
(22) Splendiani, A.; Sun, L.; Zhang, Y.; Li, T.; Kim, J.; Chim, C.-Y.; Galli, G.; Wang, F. *Nano Lett.* **2010**, *10* (4), 1271−1275.
(23) Britnell, L.; Ribeiro, R. M.; Eckmann, A.; Jalil, R.; Belle, B. D.; Mishchenko, A.; Kim, Y.-J.; Gorbachev, R. V.; Georgiou, T.; Morozov, S. V.; Grigorenko, A. N.; Geim, A. K.; Casiraghi, C.; Neto, A. H. C.; Novoselov, K. S. *Science* **2013**, *340* (6138), 1311−1314.
(24) Klots, A. R.; Newaz, A. K. M.; Wang, B.; Prasai, D.; Krzyzanowska, H.; Lin, J.; Caudel, D.; Ghimire, N. J.; Yan, J.; Ivanov, B. L.; Velizhanin, K. A.; Burger, A.; Mandrus, D. G.; Tolk, N. H.; Pantelides, S. T.; Bolotin, K. I. *Sci. Rep.* **2015**, *4*, 6608.
(25) Mak, K. F.; Lee, C.; Hone, J.; Shan, J.; Heinz, T. F. *Phys. Rev. Lett.* **2010**, *105* (13), 136805.
(26) Kim, H.; Dumcenco, D.; Frégnaux, M.; Benayad, A.; Chen, M.-W.; Kung, Y.-C.; Kis, A.; Renault, O. *Phys. Rev. B: Condens. Matter Mater. Phys.* **2016**, *94* (8), 081401.
(27) Krivanek, O. L.; Chisholm, M. F.; Nicolosi, V.; Pennycook, T. J.; Corbin, G. J.; Dellby, N.; Murfitt, M. F.; Own, C. S.; Szilagyi, Z. S.; Oxley, M. P.; Pantelides, S. T.; Pennycook, S. J. *Nature* **2010**, *464* (7288), 571−574.
(28) Cheng, Y. C.; Zhu, Z. Y.; Tahir, M.; Schwingenschlögl, U. *EPL Europhys. Lett.* **2013**, *102* (5), 57001.
(29) Mouri, S.; Miyauchi, Y.; Matsuda, K. *Nano Lett.* **2013**, *13* (12), 5944−5948.
(30) Scheuschner, N.; Ochedowski, O.; Kaulitz, A.-M.; Gillen, R.; Schleberger, M.; Maultzsch, J. *Phys. Rev. B: Condens. Matter Mater. Phys.* **2014**, *89* (12), 125406.
(31) Shin, B. G.; Han, G. H.; Yun, S. J.; Oh, H. M.; Bae, J. J.; Song, Y. J.; Park, C.-Y.; Lee, Y. H. *Adv. Mater.* **2016**, *28* (42), 9378−9384.
(32) Ponomarev, E.; Gutiérrez-Lezama, I.; Ubrig, N.; Morpurgo, A. F. *Nano Lett.* **2015**, *15* (12), 8289−8294.
(33) Zafar, A.; Nan, H.; Zafar, Z.; Wu, Z.; Jiang, J.; You, Y.; Ni, Z. *Nano Res.* **2017**, *10* (5), 1608−1617.
(34) Markov, I.; Stoyanov, S. *Contemp. Phys.* **1987**, *28* (3), 267−320.
(35) Pu, J.; Yomogida, Y.; Liu, K.-K.; Li, L.-J.; Iwasa, Y.; Takenobu, T. *Nano Lett.* **2012**, *12* (8), 4013−4017.
(36) Yomogida, Y.; Pu, J.; Shimotani, H.; Ono, S.; Hotta, S.; Iwasa, Y.; Takenobu, T. *Adv. Mater.* **2012**, *24* (32), 4392−4397.
(37) Ovchinnikov, D.; Gargiulo, F.; Allain, A.; Pasquier, D. J.; Dumcenco, D.; Ho, C.-H.; Yazyev, O. V.; Kis, A. *Nat. Commun.* **2016**, *7*, 12391.
(38) Allain, A.; Kis, A. *ACS Nano* **2014**, *8* (7), 7180−7185.
(39) Gallagher, P.; Lee, M.; Petach, T. A.; Stanwyck, S. W.; Williams, J. R.; Watanabe, K.; Taniguchi, T.; Goldhaber-Gordon, D. *Nat. Commun.* **2015**, *6*, 6437.
(40) Radisavljevic, B.; Kis, A. *Nat. Mater.* **2013**, *12*, 815−820.
(41) Schmidt, H.; Wang, S.; Chu, L.; Toh, M.; Kumar, R.; Zhao, W.; Castro Neto, A. H.; Martin, J.; Adam, S.; Özyilmaz, B.; Eda, G. *Nano Lett.* **2014**, *14* (4), 1909−1913.
(42) Fallahazad, B.; Movva, H. C. P.; Kim, K.; Larentis, S.; Taniguchi, T.; Watanabe, K.; Banerjee, S. K.; Tutuc, E. *Phys. Rev. Lett.* **2016**, *116* (8), 086601.
(43) Kastl, C.; Chen, C. T.; Kuykendall, T.; Shevitski, B.; Darlington, T. P.; Borys, N. J.; Krayev, A.; Schuck, P. J.; Aloni, S.; Schwartzberg, A. M. *2D Mater.* **2017**, *4* (2), 021024.
(44) Trusell, F.; Diehl, H. *Anal. Chem.* **1963**, *35* (6), 674−677.
(45) Bower, J. H. *Bur. Stand. J. Res.* **1934**, *12*, 241.
(46) Ling, X.; Lee, Y.-H.; Lin, Y.; Fang, W.; Yu, L.; Dresselhaus, M. S.; Kong, J. *Nano Lett.* **2014**, *14* (2), 464−472.
(47) Zhang, X.-Q.; Lin, C.-H.; Tseng, Y.-W.; Huang, K.-H.; Lee, Y.-H. *Nano Lett.* **2015**, *15* (1), 410−415.
(48) Yu, L.; El-Damak, D.; Radhakrishna, U.; Ling, X.; Zubair, A.; Lin, Y.; Zhang, Y.; Chuang, M.-H.; Lee, Y.-H.; Antoniadis, D.; Kong, J.; Chandrakasan, A.; Palacios, T. *Nano Lett.* **2016**, *16* (10), 6349−6356.
(49) Smithe, K. K. H.; English, C. D.; Suryavanshi, S. V.; Pop, E. *2D Mater.* **2017**, *4* (1), 011009.
(50) Ling, X.; Lin, Y.; Ma, Q.; Wang, Z.; Song, Y.; Yu, L.; Huang, S.; Fang, W.; Zhang, X.; Hsu, A. L.; Bie, Y.; Lee, Y.-H.; Zhu, Y.; Wu, L.; Li, J.; Jarillo-Herrero, P.; Dresselhaus, M.; Palacios, T.; Kong, J. *Adv. Mater.* **2016**, *28* (12), 2322−2329.
(51) Liu, J.; Zeng, M.; Wang, L.; Chen, Y.; Xing, Z.; Zhang, T.; Liu, Z.; Zuo, J.; Nan, F.; Mendes, R. G.; Chen, S.; Ren, F.; Wang, Q.; Rümmeli, M. H.; Fu, L. *Small* **2016**, *12* (41), 5741−5749.
(52) Hao, Y.; Bharathi, M. S.; Wang, L.; Liu, Y.; Chen, H.; Nie, S.; Wang, X.; Chou, H.; Tan, C.; Fallahazad, B.; Ramanarayan, H.; Magnuson, C. W.; Tutuc, E.; Yakobson, B. I.; McCarty, K. F.; Zhang, Y.-W.; Kim, P.; Hone, J.; Colombo, L.; Ruoff, R. S. *Science* **2013**, *342* (6159), 720−723.
(53) Chen, W.; Zhao, J.; Zhang, J.; Gu, L.; Yang, Z.; Li, X.; Yu, H.; Zhu, X.; Yang, R.; Shi, D.; Lin, X.; Guo, J.; Bai, X.; Zhang, G. *J. Am. Chem. Soc.* **2015**, *137* (50), 15632−15635.
(54) Kim, H.; Mattevi, C.; Calvo, M. R.; Oberg, J. C.; Artiglia, L.; Agnoli, S.; Hirjibehedin, C. F.; Chhowalla, M.; Saiz, E. *ACS Nano* **2012**, *6* (4), 3614−3623.
(55) Fannin, L. W.; Webb, D. W.; Pearce, R. H. *J. Cryst. Growth* **1992**, *124* (1), 307−310.
(56) Yoshimoto, M.; Maeda, T.; Ohnishi, T.; Koinuma, H.; Ishiyama, O.; Shinohara, M.; Kubo, M.; Miura, R.; Miyamoto, A. *Appl. Phys. Lett.* **1995**, *67* (18), 2615−2617.
(57) Boxhoorn, G.; Ernsting, J. M.; Stufkens, D. J.; Oskam, A. *Thermochim. Acta* **1980**, *42* (3), 315−321.

DOI: 10.1021/acs.nanolett.7b02311
Nano Lett. XXXX, XXX, XXX−XXX

Supporting Information For Suppressing Nucleation in Metal-Organic Chemical Vapor Deposition of MoS_2 Monolayers by Alkali Metal Halides

HoKwon Kim[1,2], Dmitry Ovchinnikov[1,2], Davide Deiana[3], Dmitrii Unuchek[1,2] and Andras Kis[1,2*]

[1]Electrical Engineering Institute, École Polytechnique Fédérale de Lausanne (EPFL), CH-1015 Lausanne, Switzerland

[2] Institute of Materials Science and Engineering, École Polytechnique Fédérale de Lausanne (EPFL), CH-1015 Lausanne, Switzerland

[3]Interdisciplinary Center for Electron Microscopy (CIME), École Polytechnique Fédérale de Lausanne (EPFL), CH-1015 Lausanne, Switzerland

*email: andras.kis@epfl.ch

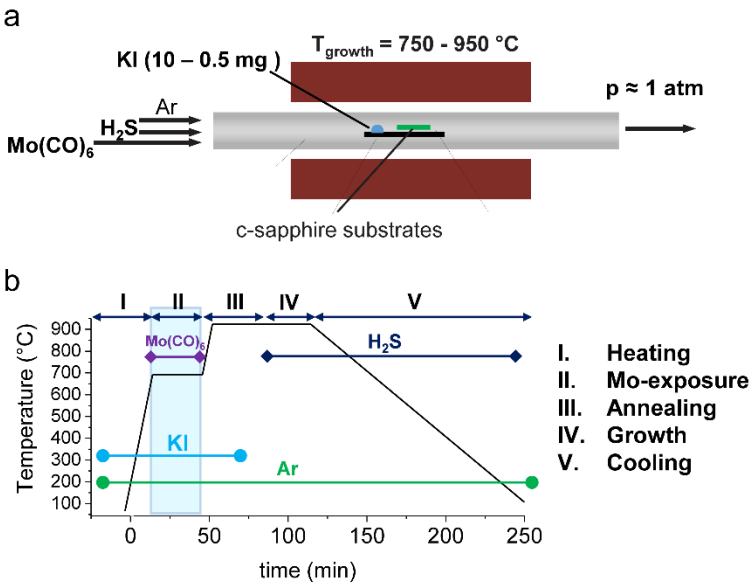

Figure S1. a) Schematic of the MOCVD system for MoS_2 growth on sapphire. b) Illustration of a typical growth process where alkali metal halide (KI) was used to suppress the nucleation density of polycrystalline MoS_2.

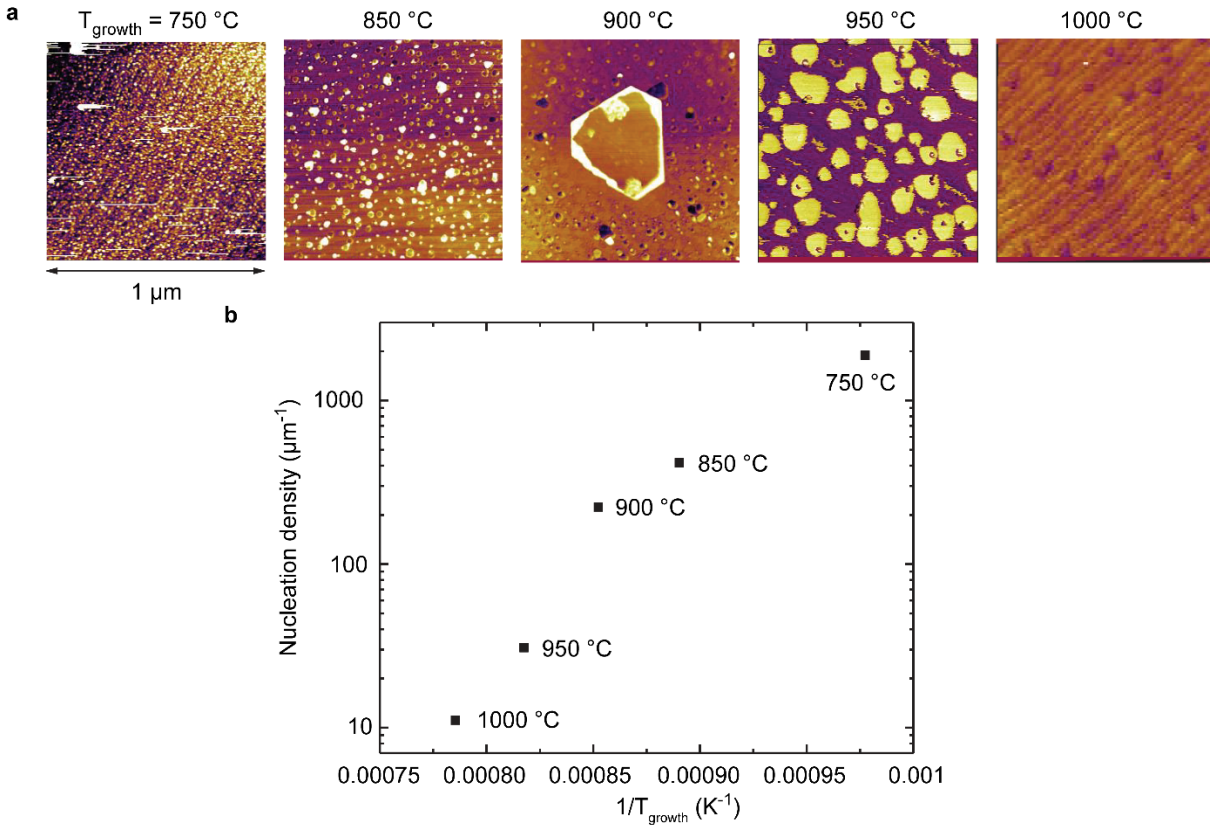

Figure S2. Temperature-dependent morphology of MoS_2 grown by MOCVD and nucleation density for the single-step growth processes without the use of alkali metal halides. a) Representative AFM height images for as-grown monolayer MoS_2 on sapphire substrate for different growth temperatures. b) Logarithmic nuclei area density versus $1/T_{growth}$ relationship based on the the samples analyzed in (a).

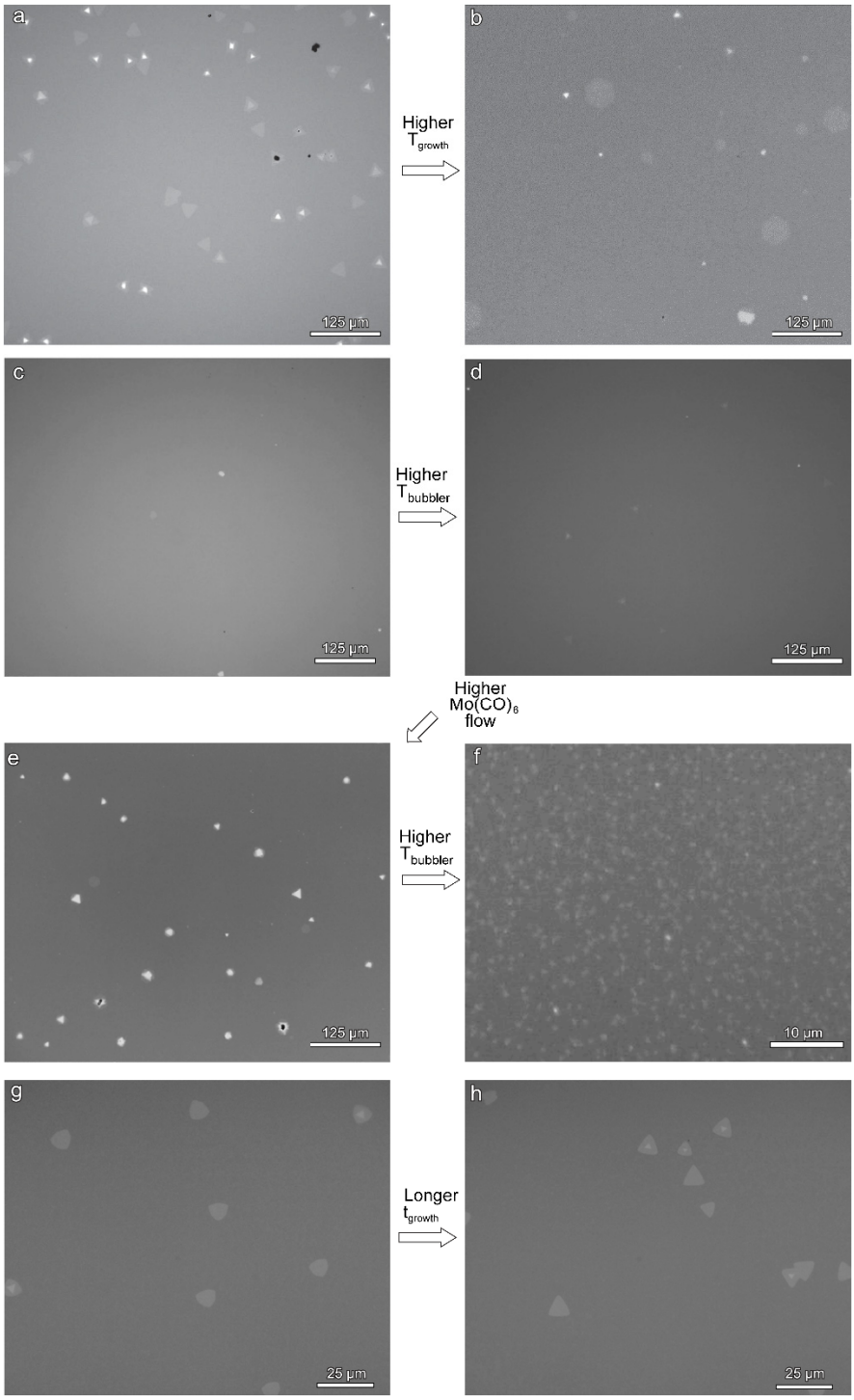

Figure S3. Morphology dependence on the growth temperature, bubbler temperature and $Mo(CO)_6$ Ar carrier flow rate. Representative optical microscope images of monolayer MoS_2 grown on sapphire for different growth conditions involving alkali metal halides (KI) for various growth parameters: a) KI 1 mg; 1.5 sccm $Mo(CO)_6$ flow rates, bubbler temp. 10 °C; 20 min pre-exposure; growth time = 30 min; 1.5 sccm H_2S; growth temp. = 900 °C. b) KI 1 mg; 1.5 sccm $Mo(CO)_6$ flow rates, bubbler temp. 10 °C; 20 min pre-exposure; growth time = 30 min; 1.5 sccm H_2S; growth temp. = 950 °C. c) KI 0.5 mg; 1.5 sccm $Mo(CO)_6$ flow rate, bubbler temp. 0 °C; 20 min pre-exposure; growth time = 30 min; 1.5 sccm H_2S. d) KI 0.75 mg;

1.5 sccm $Mo(CO)_6$ flow rate, bubbler temp. 5°C; 20 min pre-exposure; growth time = 30 min; 1.5 sccm H_2S. e) KI 0.75 mg; 10 sccm $Mo(CO)_6$ flow rate, bubbler temp. 5°C; 20 min pre-exposure; growth time = 30 min; 1.5 sccm H_2S. f) KI 1 mg; 1.5 sccm $Mo(CO)_6$ flow rate, bubbler temp. 15°C; 20 min pre-exposure; growth time = 30 min; 1.5 sccm H_2S. Note the change in the scale. g) KI 10 mg; 1.5 sccm $Mo(CO)_6$ flow rate, bubbler temp. 25°C; 20 min pre-exposure; growth time = 60 min; 1.5 sccm H_2S. h) KI 10 mg; 1.5 sccm $Mo(CO)_6$ flow rate, bubbler temp. 25°C; 20 min pre-exposure; growth time = 150 min; 1.5 sccm H_2S.

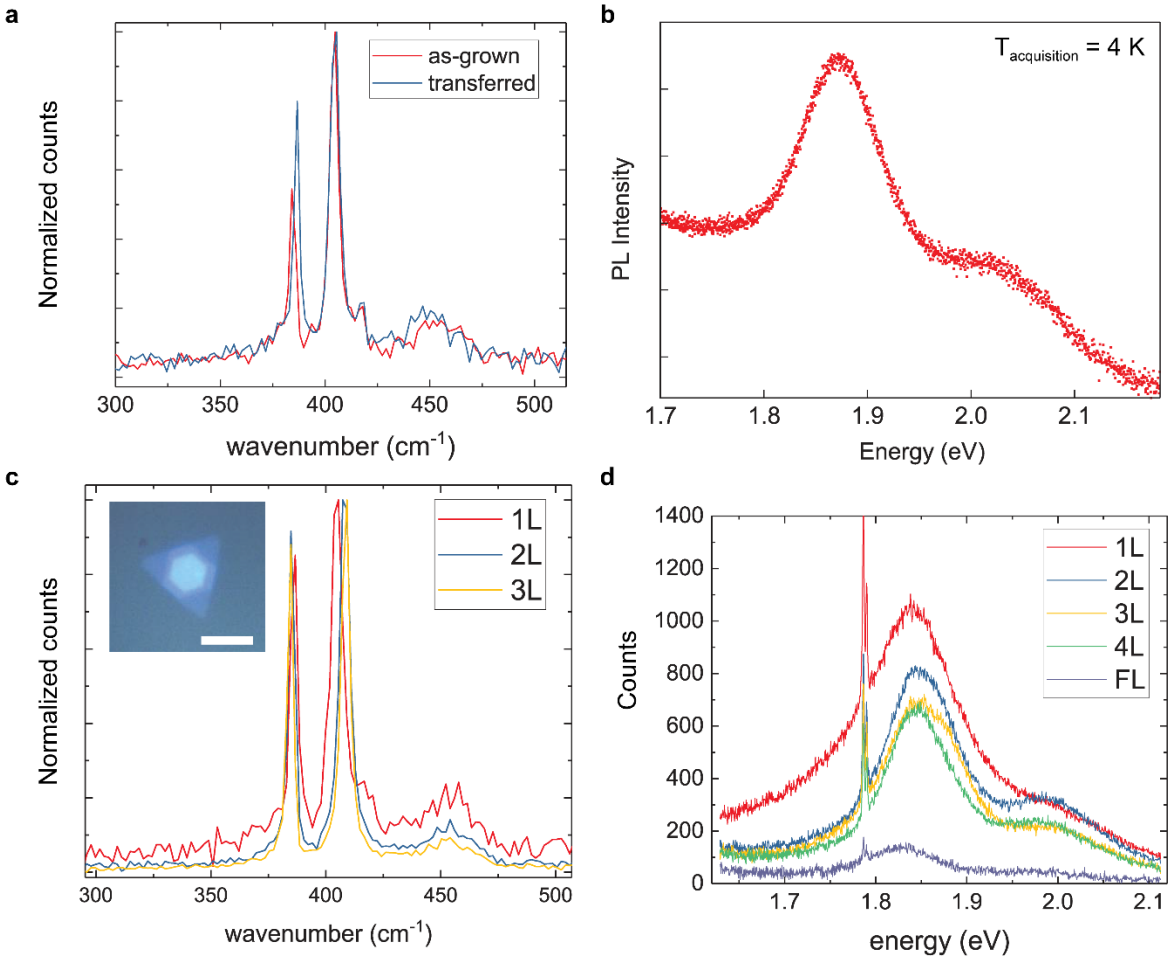

Figure S4. Raman and photoluminescence spectra of transferred samples. a) Representative Raman spectra before and after transfer. Notice the E' peak shift of ~ 1.5 cm^{-1} (corresponding to about ~ 0.3% tensile stress according to ref. 1 by D. Lloyd et al.) after transferring onto an atomically flat c-sapphire substrate. b) Low temeperature PL spectra of MOCVD MoS_2 transferred onto a SiO_2/Si substrate shows a main exciton A peak located around 1.78eV with FWHM of 78 meV. Photoluminescence measurements were performed at 4 K in an optical cryostat. MoS_2 flake was excited by a blue diode laser at 488 nm wavelength (1.52 eV) and 440 µW pumping power. c) 1L, 2L, and 3L spectra in the E' and A1' region of monolayer MoS_2 transferred onto a sapphire substrate. Excitation laser wavelength was 532 nm. Inset: a typical optical microscope image of the 1L-3L MoS_2 areas. Scale bar: 10 µm. d) Room-temperature photoluminescence spectra of 1L to FL MoS_2 transferred onto a sapphire substrate. Excitation laser wavelength was 488 nm. For each measurement the same laser spot size, power settings and acquisition times were used. Note the significant PL intensity for 2L or thicker layers suggesting a weak interlayer interaction.

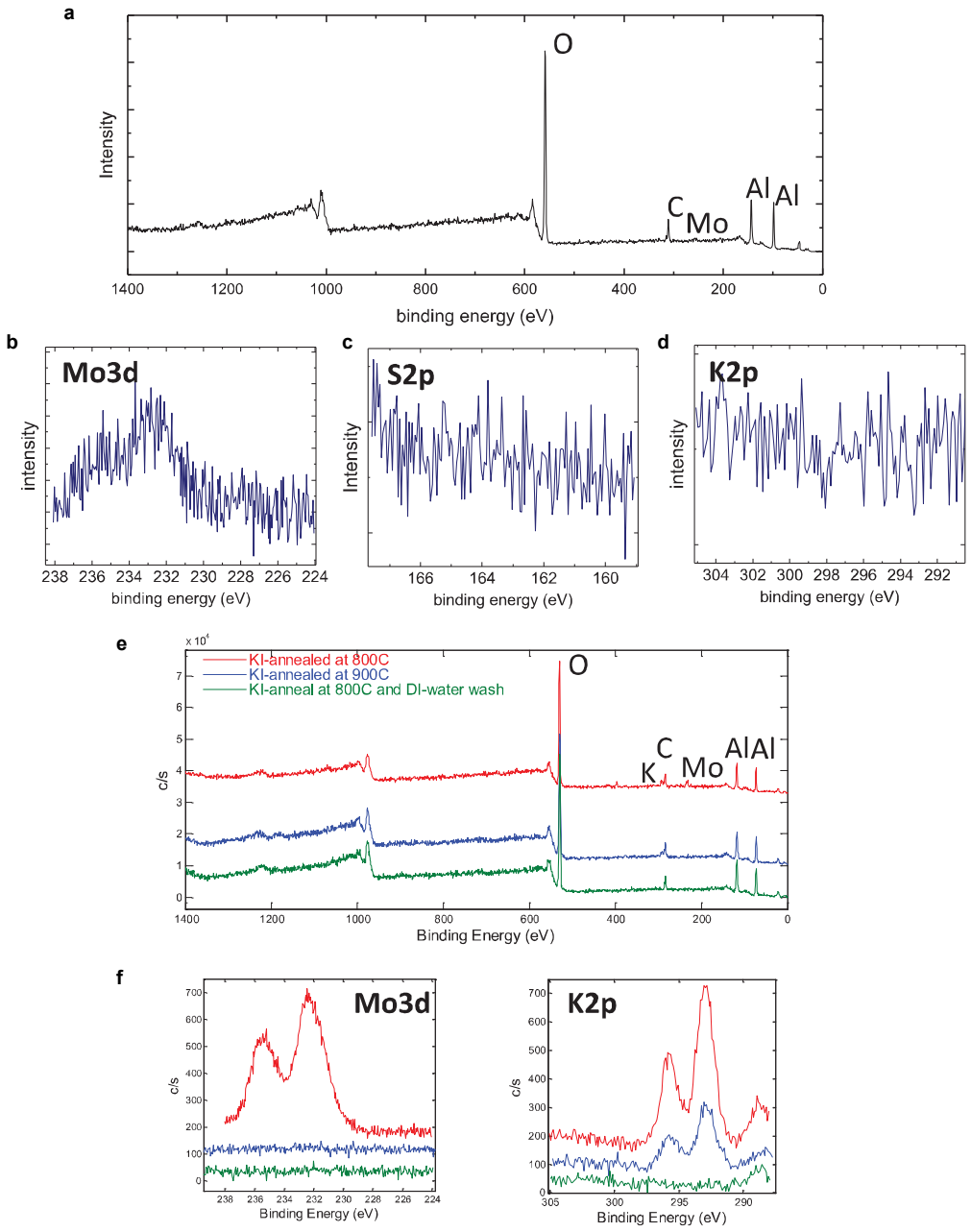

Figure S5. XPS investigation of c-sapphire susbrate after delamination (a-d), sample exposed to KI and $Mo(CO)_6$ before the growth step at 800 °C, sample exposed to KI and $Mo(CO)_6$ above 900 °C, and sample washed in DI water after exposure (e-g).

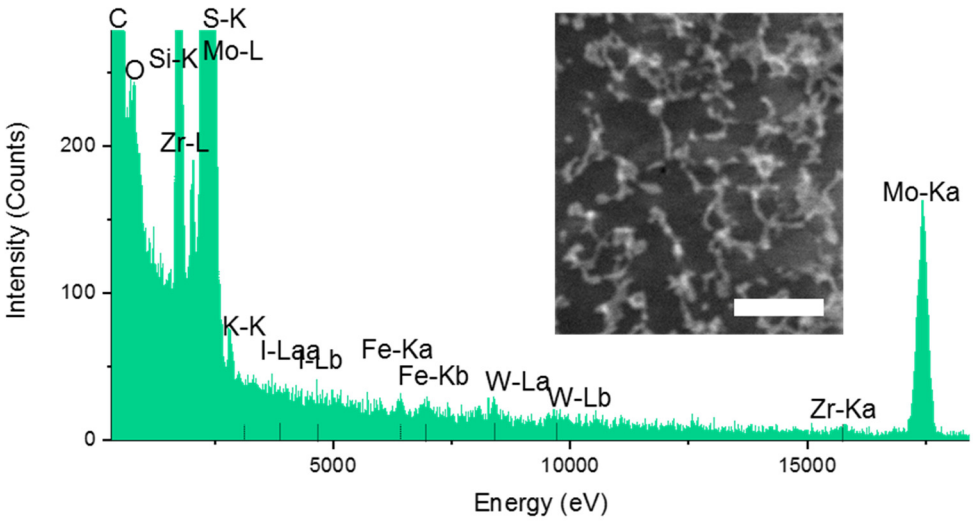

Figure S6. Representative STEM-EDX spectra of a 2L area of MoS_2 which was taken for impurity analysis. Inset: the STEM image of 2L MoS_2 area analyzed for EDX where the white, strand-like features are likely polymer (PMMA) contaminants involved in the transfer process. Scale bar: 50 nm. Note: EDX for the 1L area was also attempted but it did not provide enough signal-to-noise ratio to determine the amount of impurities for given conditions of 80 kV and < 50 nA beam current.

Electrical properties of monolayer MOCVD MoS_2

Prior to electrical characterization of the MOCVD MoS_2 EDLTs, we tested the electrical performance of our devices with solid back gates after *in situ* annealing in high vacuum (below 10^{-6} mbar). On Figure S7a we plot sheet conductivity G as a function of back-gate voltage V_g. Moderate sheet conductivity values and mobilities were measured. We notice that mobility is a carrier density dependent quantity and in the current experiment, carrier density, $n_{2D} \sim 5\times10^{12}$ cm^{-2} could be extracted from the value of $V_{th} \sim 20$V. This value is lower than the typically reported insulator to metal transition density of $\sim10^{13}$ cm^{-2}, which was observed in several experiments for monolayers of MoS_2, WS_2, WSe_2. We notice that devices with electrolyte gating exhibit much lower contact resistance values in comparison with solid-gated samples, as shown on Figure S7b.

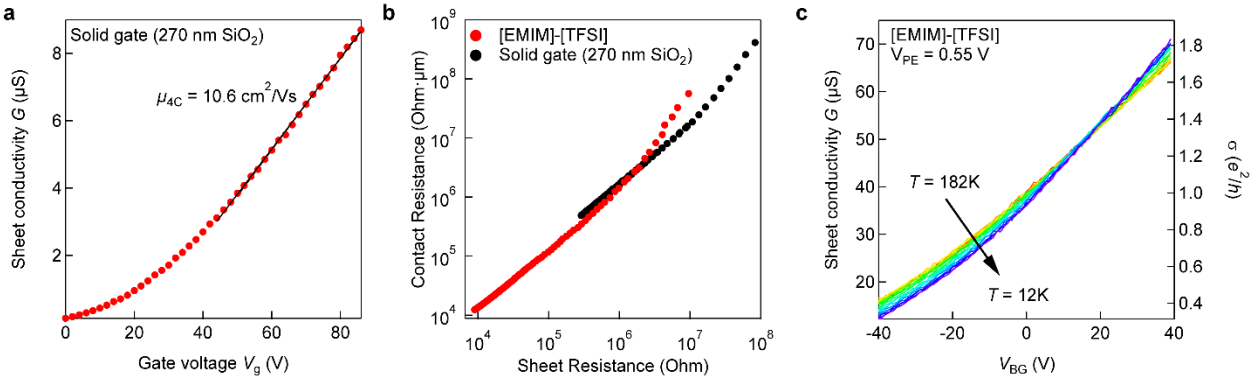

Figure S7. a) FET transfer characteristics of the device with the solid back-gate (270 nm SiO_2 dielectric) only. b) Contact resistance as a function of sheet resistance values for the solid-gating before the electrolyte deposition and liquid-gating of the same device as in (a). c) Temperature-dependent evolution of transfer characteristic of the liquid-gated device where insulator-to-metal transition was observed at ~1.3 e^2/h.

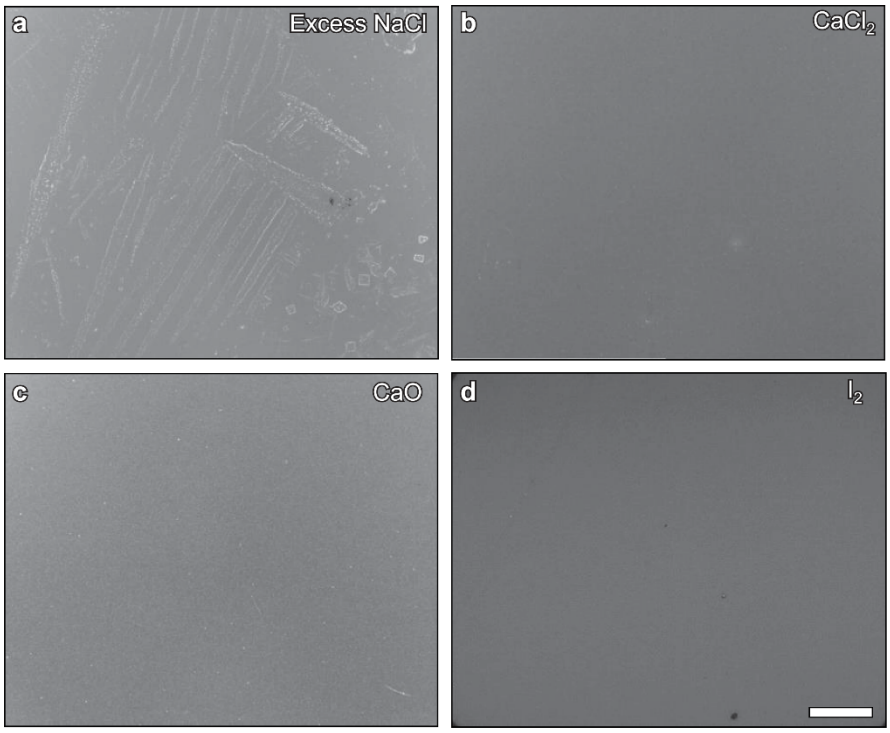

Figure S8. Optical microscopy images illustrating growth morphology with excessive NaCl (> 50 mg) (a), $CaCl_2$ (b), CaO(c), I_2 (d). Scale bar, 25 μm.

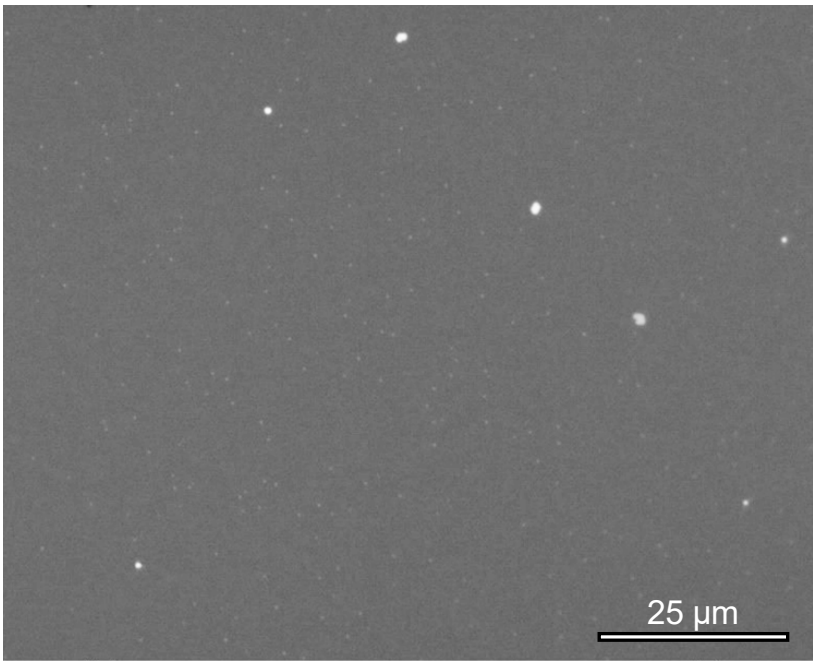

Figure S9. Optical microscopy image of a MoS_2/sapphire sample after a single-step MOCVD growth process with 10 mg of KI placed in front of the substrate at the beginning of the growth process. Notice the low coverage of MoS_2 with islands (bright dots) that appear to be smaller than 1 µm in lateral dimensions.

References

(1) Lloyd, D.; Liu, X.; Christopher, J. W.; Cantley, L.; Wadehra, A.; Kim, B. L.; Goldberg, B. B.; Swan, A. K.; Bunch, J. S. *Nano Lett.* **2016**, *16* (9), 5836–5841.